Design and operation of a von Kármán reactor for droplet breakage experiments

Krishnamurthy Ravichandar[a], R. Dennis Vigil[b], Michael G. Olsen[a,*]

[a]*Department of Mechanical Engineering Iowa State University Ames IA 50011*
[b]*Department of Chemical and Biological Engineering Iowa State University Ames IA 50011*

Abstract

The dispersion of an immiscible fluid in a turbulent liquid flow is a frequent occurrence in various natural and technical processes, with particular importance in the chemical, pharmaceutical, mining, petroleum, and food industries. Understanding the dynamics and breakup of liquid droplets is crucial in many scientific and engineering applications, as poor control and optimization of droplet systems results in significant financial losses annually. Although a theoretical background for describing droplet breakup exists, many assumptions still require experimental verification. Numerous mathematical models have been proposed to describe the rate coefficient of droplet breakup and child distribution functions. However, the validation and discrimination between models have been hindered by the lack of experimental data gathered under well-controlled and well characterized conditions. Thus, to validate the current models, novel equipment and methodology for optical droplet breakage research are required. In this work, a von Kármán swirling flow apparatus was designed and constructed to carry out optical based droplet breakage experiments under low-intensity, homogeneous turbulent flow. The methodology presented here describes the procedure for generating and controlling the size of the droplets being injected into the homogeneous turbulent flow field. The experiments involved introducing single droplets into the test section, using peanut oil to be the droplet phase and the continuous phase is water. Automated image analysis algorithms were utilized to determine breakage time, breakage probability, and child droplet size distribution for different turbulence intensities.

1. Introduction

Turbulent flow is a common phenomenon in a range of industrial fields, including the chemical[18, 20], food, petroleum, and pharmaceutical industries[14, 16, 22, 22]. In multiphase systems that operate under turbulent conditions, high rates of mass and heat transfer are often required. This includes the separation of two-phase flows consisting of two immiscible components, such as oil-in-water or water-in-oil dispersions. In these systems, droplet

*Corresponding author
URL: mgolsen@iastate.edu (Michael G. Olsen)

breakage and coalescence play a significant role since they affect the interfacial area between the continuous and dispersed phases, which, in turn, affects mass and heat transfer between the phases. Therefore, understanding the mechanism responsibile for droplet breakage is crucial to the understanding of interphase transport in liquid-liquids systems.

The predominant method for predicting the size evolution of droplets suspended in a second continuous turbulent liquid phase is to carry out computational fluid dynamics (CFD) simulations that include population balance equations (PBEs) describing droplet growth and fission due to coagulation and breakage mechanisms. In the absence of coagulation, droplet breakage in a closed spatially homogeneous system can be described by the following transport equation for the concentration of droplets with volume p at position $\vec{x}$ and at time t, represented by $C(p, \vec{x}, t)$, and given by

$$\frac{\partial C}{\partial t} + \nabla \cdot (C\vec{u}_d) = D_e \nabla^2 C - a(p)C + \int_p^\infty a(q)b(p|q)C\partial q \tag{1}$$

In the above equation $\vec{u}_d$ is the droplet phase velocity, D_e is the effective diffusion coefficient, $a(p)$ represents the rate coefficent describing breakage of droplets of size p, and $b(p|q)$ is the conditional probability that a child droplet with volume p is produced upon breakage of a parent droplet with volume q. Hence, the second term on the right side of (5) represents loss of droplets of volume p due to breakage, and the last term represents gain of droplets with volume p due to breakage of larger sized droplets. The functions a and b comprise the droplet breakage kernel, and they depend in general not only on the sizes of the parent and child droplets, but also upon the flow conditions, the breakage mechanism, and fluid physical properties.

Although numerous mathematical expressions for breakage rate coefficient $a(p)$ and child distribution functions $b(p|q)$ have been proposed, validation and discrimination between models has been hindered by a lack of experimental data gathered under well controlled and characterized conditions. For example, many droplet breakage studies have been performed using stirred tanks or other devices that generate heterogeneous turbulence, and as a consequence it is difficult to accurately determine droplet breakage rate dependence on flow parameters such as turbulent dissipation rate which can be difficult to precisely determine in a heterogenous flow field. Other droplet breakage experiments have suffered from the inability to gather sufficient data to resolve important droplet breakage features such as breakage time, breakage probability, and child droplet probability distribution functions. Some previous experimental investigations of droplet breakage are summarized below.

Konno et al.[11]conducted an initial experimental investigation into the breakage of individual droplets and reported mean values for the number of resulting child droplets, ranging from 2.6 to 4.4. However, they did not establish a relationship between the size of the parent droplet and the distribution of daughter droplets. Furthermore, from a statistical standpoint, the amount of data collected was considered inadequate, as there were fewer than 100 instances of droplet breakage recorded for most of the tested conditions.

Bahmanyar and Slater[26] conducted a study on the breakage of individual droplets using a revolving disk contactor. However, they faced challenges in accurately determining the

specific times at which the droplets underwent breakage due to the limitations of their measuring techniques. The capillary and video approaches they employed lacked the necessary temporal precision to capture the precise breaking times of individual droplet events.

Galinat et al.[12, 13]conducted breakage experiments involving single n-heptane droplets within the diameter range of 1.5-3mm. They utilized commercial software to measure droplet sizes, breakage times, and breakage probabilities. Their observations revealed that an increase in droplet diameter and flow velocity resulted in an elevated breakage probability. However, the study did not offer a comprehensive explanation or definition of the experimental parameters employed in the research.

Ashar et al. [1] conducted a study on single droplet breakage in a stirred tank, focusing on breakage probability and average daughter droplet numbers. Notably, the study lacked a detailed explanation of the statistical methodology employed. The authors introduced the concept of "deformation time," representing maximum droplet deformation, which occurred earlier than the initial breakage. The experiments utilized rapeseed oil droplets and deionized water, investigating 285 breakage events at different Turbulence Dissipation Rate (TDR) levels determined through PIV analysis. However, the study did not provide information regarding Turbulent Kinetic Energy (TKE).

Andersson and Andersson [2, 3] examined the fragmentation of individual oil droplets (dodecane or octanol) dispersed in water using a static mixer. They reported the breakage time as a function of the turbulence dissipation rate. The distribution of daughter droplet numbers for dodecane droplets was provided for two different turbulence dissipation rates, based on approximately 50 instances of breakage events involving 1mm diameter mother droplets. However, the study did not include any additional statistical analysis beyond these findings.

Solsvik and Jakobsen [28, 29] examined the breakage of individual oil droplets in a stirred tank. They determined the breaking time and the distribution of daughter droplets based on the size of the mother droplet for different oil types (toluene, petroleum, dodecane, and 1-octanol) dispersed in distilled water. Each oil type had between 180 and 250 recorded breakage events, with the mother droplets divided into groups with a 0.5 mm width. However, the study did not include any statistical analysis in their findings.

A number of researchers have investigated the breakup of droplet swarms [36–39], however, the present investigation considers only single droplet breakage events, thus comparison with those results is inappropriate here.The following sections explain an experimental system and procedure that can address the shortcomings of prior studies on droplet breakage. To capture multiple droplet breakage incidents, the system utilizes high-speed photography in a von Kármán swirling flow test section. This test section creates a region of homogeneous and isotropic turbulence around the droplet injection port, and it enables accurate regulation of the size of individual parent droplets introduced into the breakage region. Additionally, this work presents an algorithm for measuring breakage parameters from video footage of breakage events, including breakage time, likelihood of breakage, and distribution of child droplets. Finally, the experimental and data analysis techniques are demonstrated in experiments that collect and analyze data on breakage of peanut oil droplets in water.

2. Experimental Methodology

2.1. Experimental Configuration

An illustration of the droplet breakage experimental configuration is presented in Fig: 1. A closed fluid supply circuit is used for filling and emptying the test section with deionized water. The von Kármán box (1) is illuminated by a LED tube light fixture (2) and diffuser (3) so that high-speed video can be used to capture droplet breakage events. Two syringe pumps, (4) and (5), are connected to a T-junction fitting (6). A reservoir supplies deionized water to one of the syringe pumps (4). The deionised water acts as the carrier fluid. Individual organic droplets are generated in the T-junction by using the second syringe pump (5) to control the flow rate of the dispersed phase. Varying the flow rates of the two syringe pumps allows for the generation of droplets of various sizes. Each individual generated oil droplet is then carried via flexible tubing into an injection needle inside the von Kármán cell. A high-speed camera (7) is positioned opposite of the light source and orthogonal to the flow cell impellers The various components of the system discussed above are described in detail in the sections that follow.

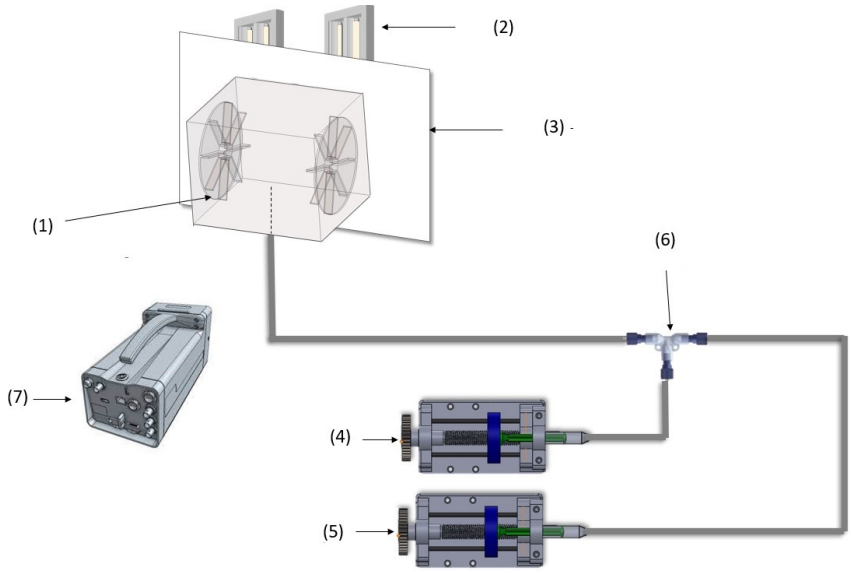

Figure 1: Schematic of the experimental setup.

2.2. von Kármán Box

The von Kármán geometry, which refers to the flow between two finite counter-rotating disks that are enclosed by a cylinder, is significant in many industrial devices[31, 33]. One example is the use of counter-rotating turbines to drive fans in gas-turbine aero-engines [32, 33]. Additionally, this setup is frequently employed to examine essential aspects of turbulence, particularly magneto-hydrodynamic turbulence [31]. The device utilized in this study is a von Kármán flow apparatus, which is similar to the one used by De La Rosa Zambrano et al [15]. However, the current appartus makes use of a tank with square rather than circular cross section to reduce the distortive effects of refraction.

2.3. Experimental Setup

Designing and constructing the von Kármán flow cell was an iterative procedure in which many shortcomings were identified and overcome. Here, we document this iterative procedure so that future researchers can construct a robust flow cell more easily. The von Kármán tank was designed to have interior dimensions of 200.15 mm x 250.95 mm x 206.502 mm (10.4 liter volume) and be filled with deionized water as the continuous-phase fluid. The first iteration of the tank was constructed of polycarbonate and had a single lid, meaning only the top of the tank could be removed. Polycarbonate was selected as the material of choice due to its toughness and high resistance to impact and chemicals. Furthermore, its transparency facilitates unrestricted optical access from all sides. The tank was equipped with a detachable lid to allow cleaning of the interior between experiments. Nevertheless, this approach had a significant drawback in that the absence of a tight seal caused air to enter the tank, leading to the creation of air bubbles inside the tank.

The second major flaw with the design was that as the tank was filled with the continuous phase, there was no easy outlet for the displaced air from the tank to leave during the filling procedure. Consequently, the tank became pressurized, resulting in damage to the polycarbonate material and also an increase in air bubbles in the tank. The third flaw with this first iteration was that the polycarbonate material is porous, particularly in fused areas, such as the edges of the tank. This also allowed air to enter the tank, particularly when the impellors rotated at high speeds.

The second design iteration addressed the shortcomings of the first reactor by adding flanges to the top and bottom of the reactor. This allowed for a compression-fit, gasketed lid design, as can be seen in Fig: 2.

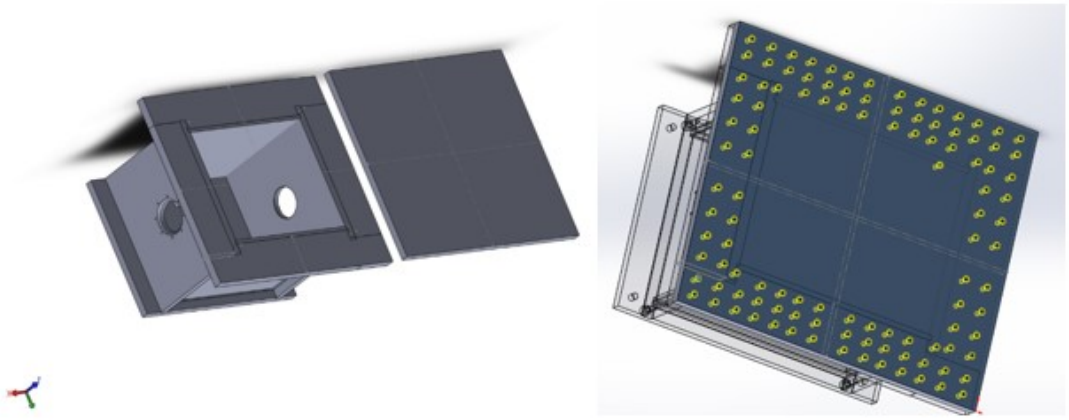

Figure 2: (a) Second iteration of the von Kármán reactor and (b) reactor lid design.

Fig 3 shows schematics of the final iteration of the Von Karman reactor.In order to ensure watertight seals for the tank illustrated in Fig: 4, Durometer 30 compression gaskets and

160 1/4-inch Allen screws were employed to secure the top and bottom lids. Additionally, 3M 4200 Marine sealant was applied to the edges of the tank to seal the porous holes in the polycarbonate, ensuring that there was no air leakage from the edges of the tank. A 1/8-inch hole was drilled into the top lid of the tank, which enabled the installation of a 300mm long, 30mm diameter pipe to serve as a "chimney." The chimney facilitates the evacuation of air as the tank is filled with the continuous phase, preventing pressurization of the tank.

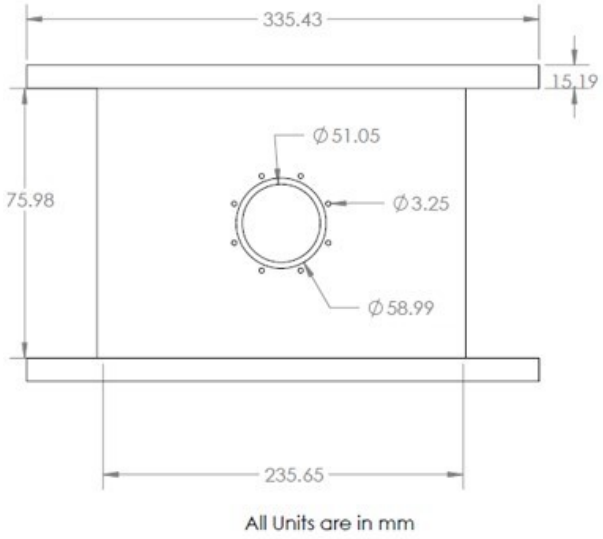

(a) Side View

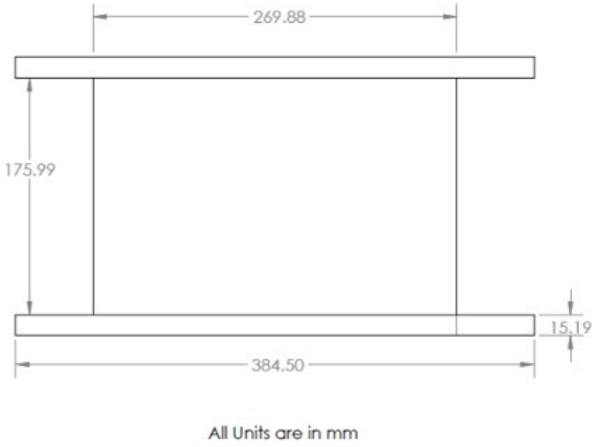

(b) Front View

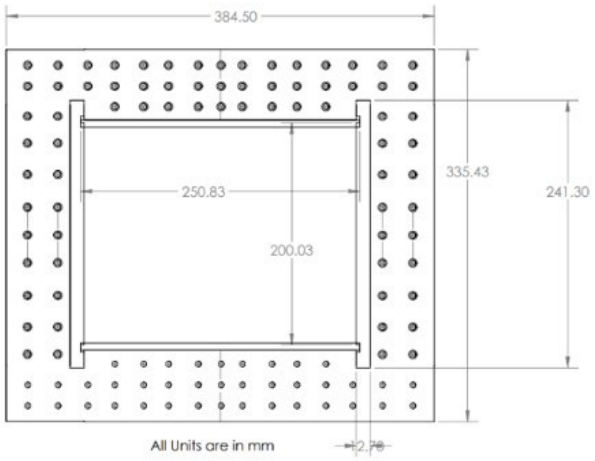

(c) Top View

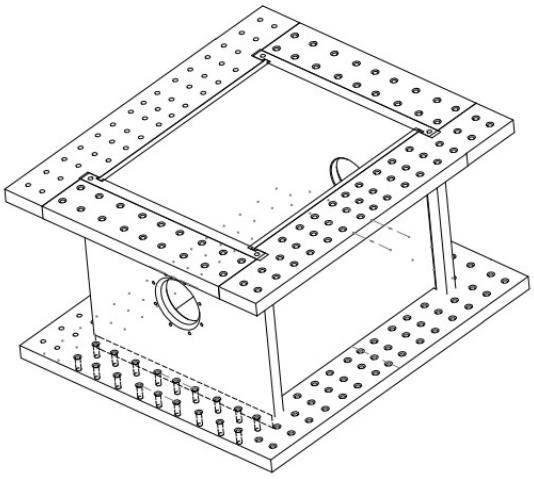

(d) Perspective View

Figure 3: Schematics of the von Kármán reactor.

The reactor was then mounted on a stainless-steel frame with dimensions 216 mm x 267 mm x 206.5 mm as can be seen in Fig: 5. The steel frame greatly reduces tank vibration when the impellors are rotated at high rpm.

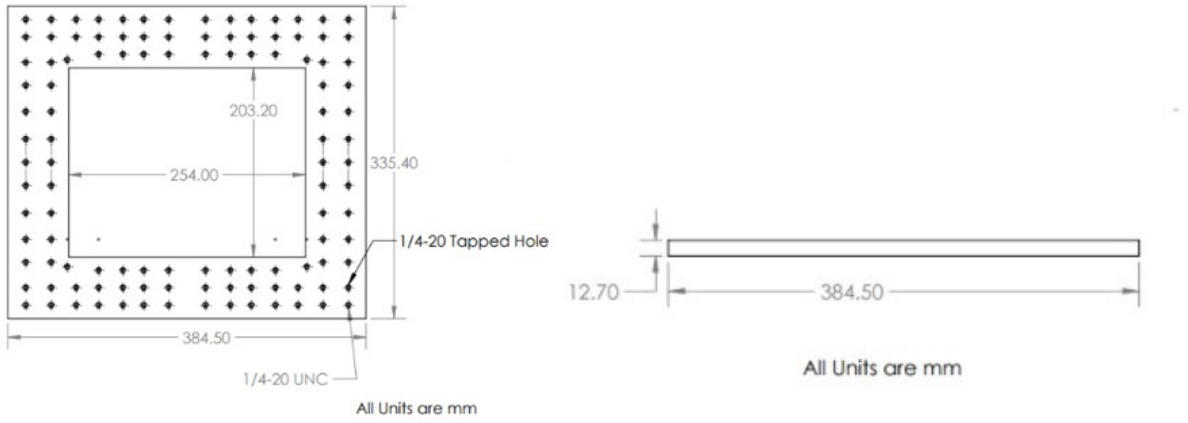

(a) Top View **(b)** Side View

Figure 4: Schematics of the lid of the von Kármán reactor.

The steel frame is held together by a steel bracket which connects the legs of the frame with the base, as seen in Fig:5a. These brackets provide structural support and rigidity to the base of the frame. Additional brackets were added to the legs which allows the box frame to be mounted to a NewPort optical table as can be seen in the top view shown in Fig:5b. The optical table utilizes the Integrity 4 VCS system, which incorporates precision-tuned mass damping (TMD) technology with two tuned dampers to eliminate resonances in the table.

2.4. Sizing of Motor and Design of Impeller and Shaft

Two counter-rotating impellers with a diameter of 200 mm were installed on either sides of the test section. An impeller drive shaft is used to connect the DC motor to each impeller within the test section .

From the schematic shown in Fig. 6 it can be seen that the main purpose of the rotary shaft collar is to prevent air and water leakage. In order to ensure efficient transmission of the power from the motor to the impeller, the drive shafts are fitted with two bearings which are rated for speeds up to 10,000 rpm . The design of the impeller shaft is illustrated in Fig. 6. The impellers shown in Fig. 7 are driven by DC stepper motors that are rated for up to 300 oz-in of torque. The selection of these motors was mainly due to their computer-controlled stepping feature that allows precise regulation of the speed, thus providing excellent control over the turbulent dissipation rate within the test section. The motors are mounted on a steel structure which is then connected to the impeller shafts via Oldham coupling discs.This helps reduce the overall vibration and noise experienced by the test section.

Demonstrating the homogeneity of the breakage region within the test section is critical because the von Kármán flow cell was purposefully designed and constructed to minimize spatial heterogeneity and establish a homogeneous isotropic turbulence region where droplet breakage can occur. To achieve this, 3-dimensional simulations were carried out with the

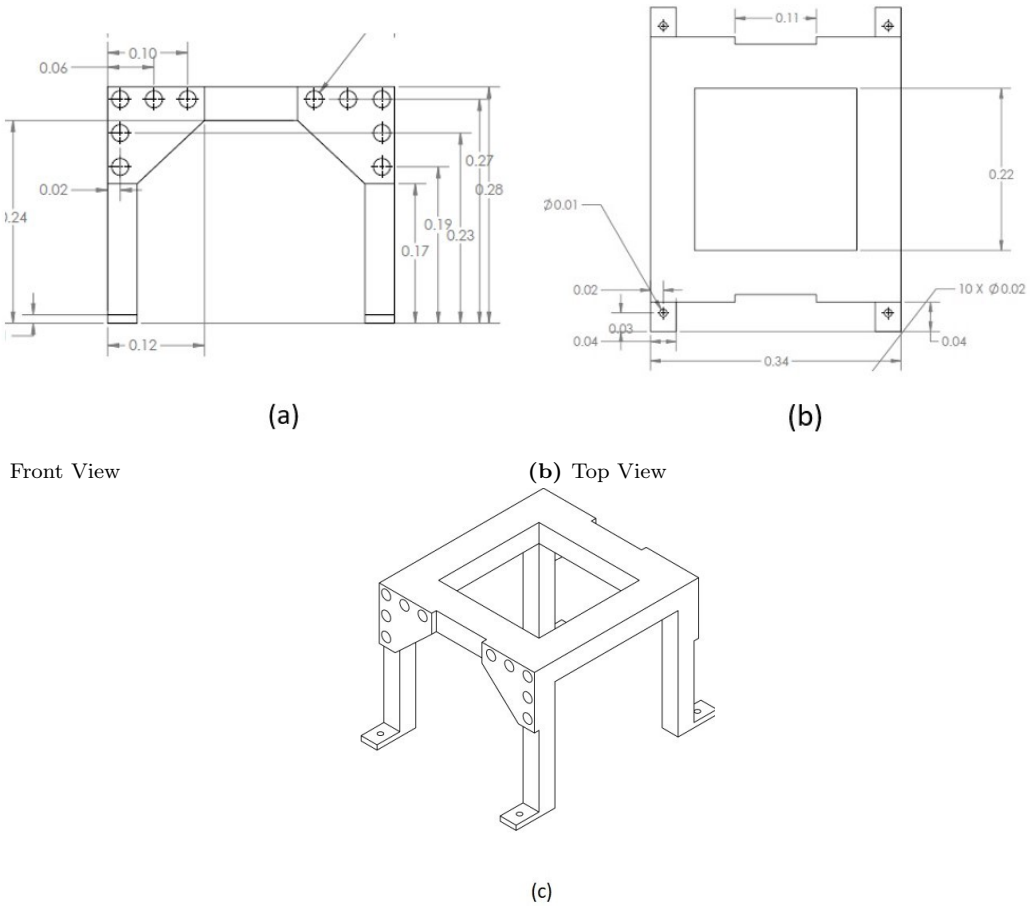

(a) Front View

(b) Top View

(c) Isometric View

Figure 5: (a) Side view of von Kármán reactor support struts (b) top view of reactor support struts and (c) Represent isometric view of the support frame

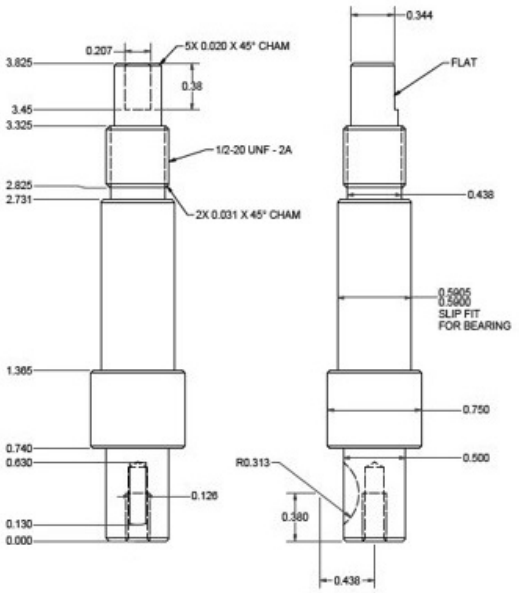

(a) Impeller Shaft Housing

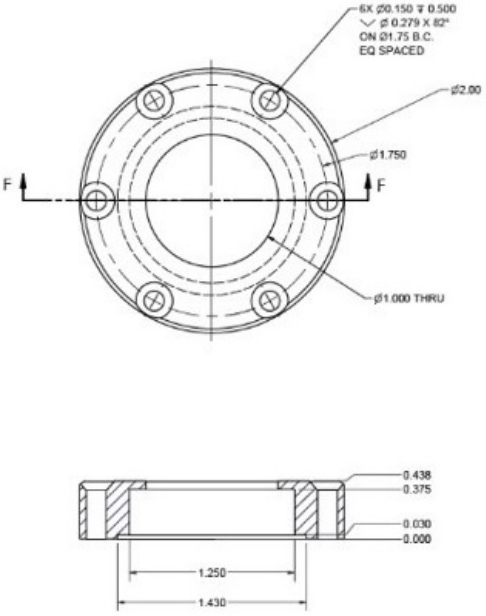

(b) Seal Collar

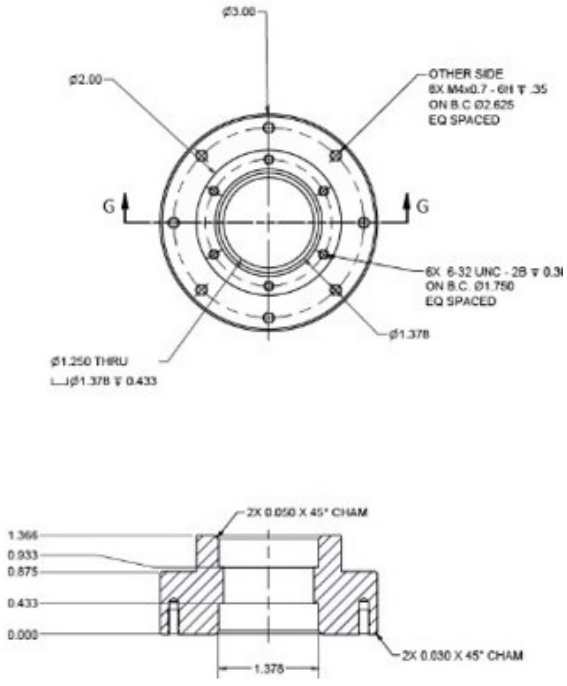

(c) Shaft Housing

Figure 6: Drawing of the impeller shaft housing, seal collar and shaft.

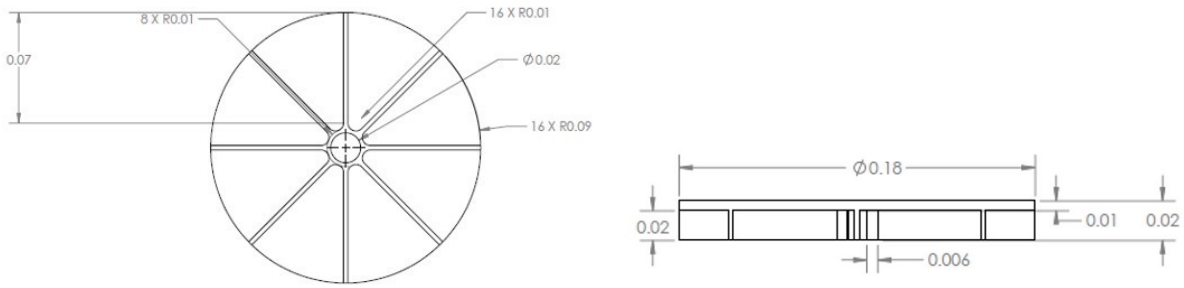

(a) Top View **(b)** Side View

Figure 7: Top and side view schematic of the impeller.

k-ε and Reynolds stress turbulence models using Ansys FLUENT 2021 computational fluid dynamics software [4, 10, 17, 21]. To assure accuracy, grid convergence experiments were performed, and a final structured linear mesh with 817,170 nodes and nearly 2.2 million elements were created.

Within the Von Kármán reactor [35], these flow modes encompass two distinctive phenomena: a poloidal pumping effect generated by centrifugal forces at the rotating disks, causing fluid expulsion and subsequent circulation along the centerline, and a shearing mode induced by the opposing directions of disk rotation . These complex flow dynamics, as depicted in Figure 8, reveal a significant feature – non-bilateral symmetry. In the context of the dynamic system under scrutiny, a fascinating phenomenon emerges, referred to as symmetry breaking, with particular emphasis on the central transverse plane. In essence, this signifies that the boundary between the poloidal pumping cells has the potential to shift along the rotation axis, introducing asymmetry into the system. Intriguingly, this asymmetry often coincides with the formation of substantial vortices within the shear layer. It is worth highlighting that only a limited number of researchers have observed long-term stationary flow modes that maintain symmetry relative to the central transverse plane.

Figure 8 shows a contour plot of the estimated turbulent dissipation rate and turbulent kinetic energy. According to Figs. 8a and 8c, the highest turbulent dissipation rate is at the tip of the impeller, and the dissipation rate gradually decreases as one approaches the middle of the tank where droplets are injected. To determine homogeneity at the center of the test section (that is within the measurement region where individual droplets are injected), a sphere with a volume of 65.44 cm^3 and a diameter of 5 cm was considered at the center of the test section, and the turbulent dissipation rate was calculated within this volume. The mean turbulent dissipation rates were found to be 0.08251 m^2s^{-3} and 0.235 m^2s^{-3} for rotation speeds of 65 and 165 rpm, respectively. It was found that within this sphere the local dissipation did not deviate by more than 5% from the mean dissipation rate.

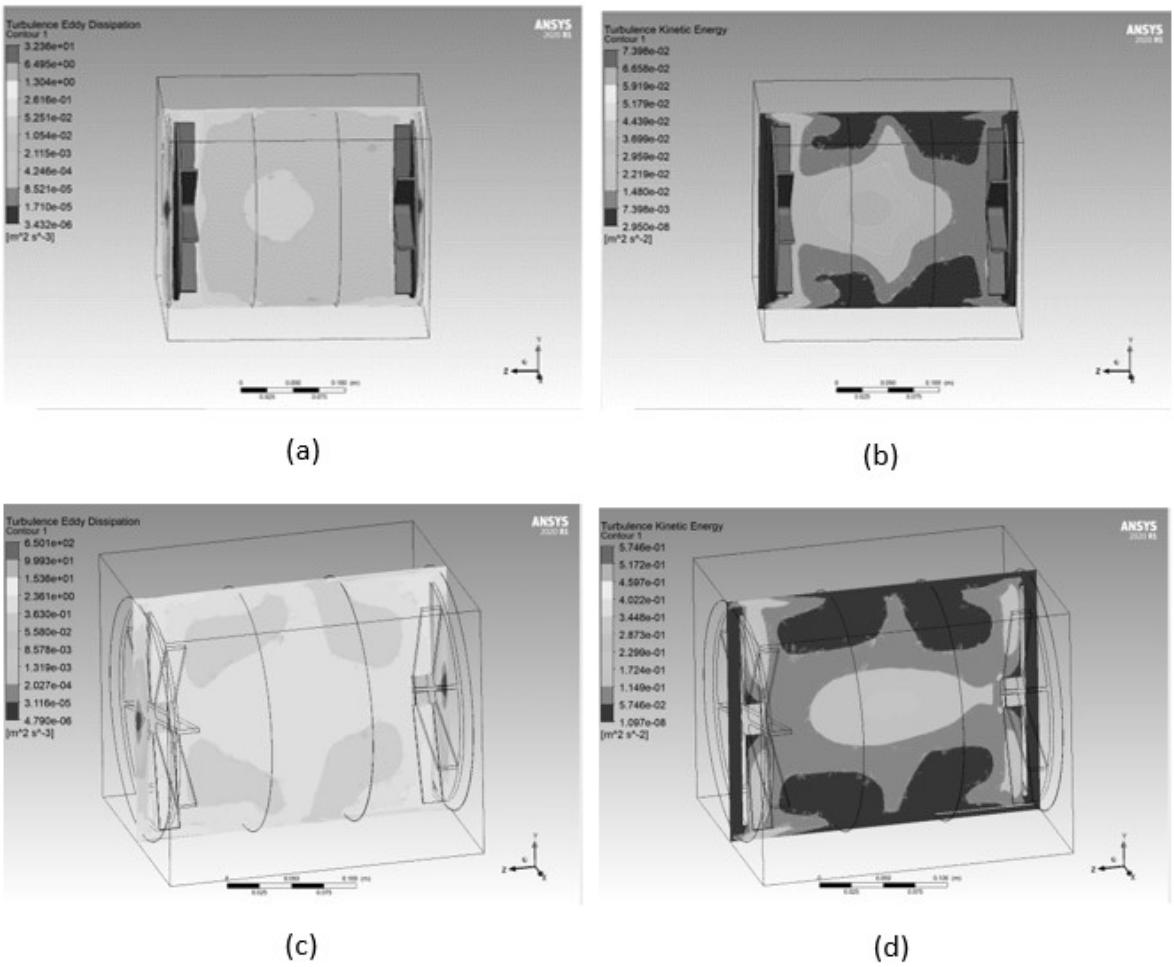

Figure 8: (a) a plot of the average ε for an impeller speed of 65 rpm, in a vertical plane perpendicular to the impellers and passing across the impeller axis of rotation. (b) a plot of the turbulent kinetic energy for an impeller speed of 65 rpm. (c) contour plot of the average ε for an impeller speed of 165 rpm. (d) contour plot of the turbulent kinetic energy for an impeller speed of 165 rpm.

2.5. Droplet Generation

A syringe pump method was used to generate the droplets injected into the test section. This approach employs two syringe pumps to control the flow rate of the fluids being discharged and a T-junction to create the droplets. An IDEX P-633 T-junction, with a length of 9.40 mm and an inner diameter of 1.27 mm is utilized to mix the two fluids and generate the droplets. The syringe pumps were configured such that one controlled the flow rate of the continuous phase (water), which acted as the carrier fluid for the droplets, while the other was responsible for providing the droplet phase (oil). By varying the flow rates of the water and oil, different diameter droplets can be generated. This droplet generation method has proven to be effective in producing droplets as small as 1 mm in diameter.

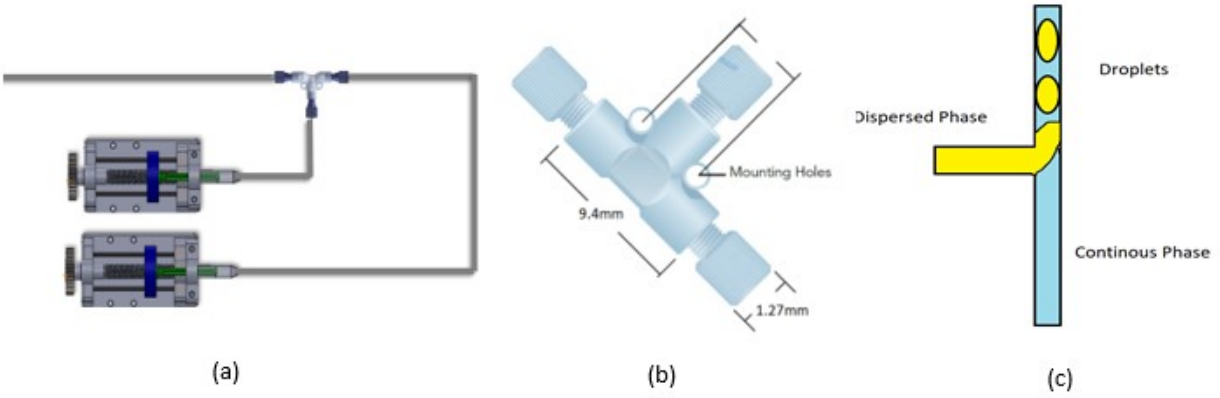

Figure 9: Illustrations of the droplet generation section showing (a) the two syringe pumps and tubing (b) schematics of the T junction (c) Droplet generation within a T junction

To demonstrate the droplet generation and injection method, peanut oil was selected as the test fluid for droplets. Approximately 0.5 ml of non-water-soluble blue dye was added to 100ml of oil resulting in the droplets having enhanced visibility. To determine if the dye affected interfacial tension and viscosity, measurements were taken for these quantities in the dyed oil. A falling ball viscometer was used to measure viscosity, while the pendant drop method was used to measure the liquid-liquid interfacial tension.Table 1 shows the obtained values for viscosity and interfacial tension of the dyed peanut oil. The measurements were found to be consistent with values reported in literature for undyed peanut oils.

After being generated, the droplets are transported through a teflon coated PTFE tube with a 1/16-inch diameter. The stainless-steel needle is connected to a 1/16-1/8 inch adapter which enters the tank through its bottom wall. Once inside the tank, the droplets pass through a 22-gauge needle with its tip located at the center of the tank. This injection needle has a length of 25.4mm and inner and outer diameters of 0.41 and 0.74 mm, respectively.

2.6. Camera and Image Acquisition

The Photonics FASTCAM-APX RS camera is used to capture images of the oil droplets. The camera is fitted with a Sigma 50 mm macro lens that can achieve magnifications ranging

Table 1: The densities, interfacial tensions, and viscosities of the droplet test fluids were measured and presented in the table. Additionally, values reported in previous studies from the literature are also provided.

Oil	**Density** (kg/m^3)	**Interfacial Tension (N/m)**	**Literature Interfacial Tension (N/m)[29, 30]**	**Viscosity (mPas)**	**Mean Literature Value Viscosity (mPas)[29, 30]**
Peanut Oil	910	0.025	0.022-0.032	80.6	70

from 1 to 5. The camera is tightly mounted on steel shelves and screwed tight to reduce vibrations. The shelves can be moved up and down to position the cameras at different heights in relation to the von Kármán flow chamber. The lens has a minimum facal distance of 18.88 mm, allowing the camera to be placed near the wall of the reactor. The field of view can be changed by adjusting the distance of the lens from the object plane or by adjusting the magnification

The images captured in this investigation have a square-shaped field of view with side lengths measuring 117 mm. The wide depth of field of approximately 33 mm was essential to keep the droplets in focus while they traveled through the test section during data acquisition due to the f/32 aperture used in the recording process. The Photonics camera has the ability to capture 2048 images of 1024 X 1024 pixels at full resolution, with a maximum speed of 2 kHz.The fast capture speed enables temporal resolution of the most rapid breakage events. During measurement, the droplets were being injected close to the center of the test section thus, the center section calibration factor was used for obtaining the size and position of the droplets. The spatial resolution of 0.115 mm means that one pixel on the image corresponds to a square of 0.115 by 0.115 mm.The high-speed camera is controlled remotely using a pc, and a video acquisition card is mounted to the motherboard of the pc. This allows for remote triggering of the high-speed camera, which ensures that the camera is only active when droplets begin to leave the tip of the needle.

2.7. Lighting

To capture the motion of moving droplets, high-speed imaging necessitates strong and sustained lighting as the required exposure time is very short. In this study, an exposure time of 1/600 s and a frame rate of 250Hz were used to capture droplet breakage events. The test section was illuminated through the opposing side relative to the camera using a portable light fixture with four 24 Watt fluorescent tube lights placed 0.2 m from the test section. White poster paper with an area of 864 cm^2 positioned at a distance of 0.05 m from the light source diffused the light to ensure that it was soft and evenly distributed across the fluid test section.

3. Image Processing

Validation of droplet breakage models requires, at a minimum, the measurement of the following quantities associated with breakage of a droplet with known size: (1) The mean time required for the droplet to undergo breakage, (2) the fraction of droplets of a given size that undergo breakage within a fixed observation volume, and (3) the distribution of child droplets produced from breakage of a parent droplet. Image sequences showing droplets undergoing deformation, stretching and rupture can also provide useful quantitative information for validating and improving breakage models.

As described previously, the FASTCAM-APX RS high-speed camera is capable of capturing a sequence of 2048 images at speeds up to 2 kHz at full resolution (1024 x 1024 pixels). A sequence of these high-speed images provides detailed tracking of droplet motion and deformation through the test section, with the time separation between each sequential frame dependent on the high-speed camera's frame rate. Sequences of image frames obtained from a large ensemble of droplet breakage events are processed using custom Matlab-based software to extract information concerning breakage time, breakage probability, and child distribution function. This image processing procedure implements a thresholding procedure to remove background noise and to binarize images, followed by image segmentation to determine the distribution of connected pixels, from which it is possible to quantify droplet size and shape, to detect the moment of droplet scission, and to measure the size and shape of child droplets.

3.1. Size Calibration

Calibration of droplet size in the images is achieved by making use of the known (measured using a micrometer) exterior diameter (0.74mm) of the injection needle tip. Specifically, by capturing an image of the needle tip, the number of pixels across the needle diameter provides the needed conversion factor, which for the experiments reported here is given by

$$C_{pixel-mm} \approx 0.115 \ \frac{\text{mm}}{\text{pixel}} \tag{2}$$

During measurement, the droplets were being injected close to the center of the test section thus, the center section calibration factor was used for obtaining the size and position of the droplets. To determine the uncertainty in the droplet size measurement, the magnification at the front and back of the depth of field was also calculated:

$$C_{front_{pixel-mm}} \approx 0.113 \ \frac{\text{mm}}{\text{pixel}} \tag{3}$$

$$C_{rear_{pixel-mm}} \approx 0.118 \ \frac{\text{mm}}{\text{pixel}} \tag{4}$$

This results in magnification uncertainty of approximately $\pm$ 2.2%.

3.2. Image Thresholding

The process of image thresholding involves subtracting a background reference image from each acquired grayscale image. This is done to eliminate fixed imperfections, such as dust particles or air bubbles that may be present on the wall of the fluid test section. Subsequently, image contrast is increased and binarization is performed using Otsu's method [11, 30]. Example before and after results of the image processing procedure are shown in Fig: 10.

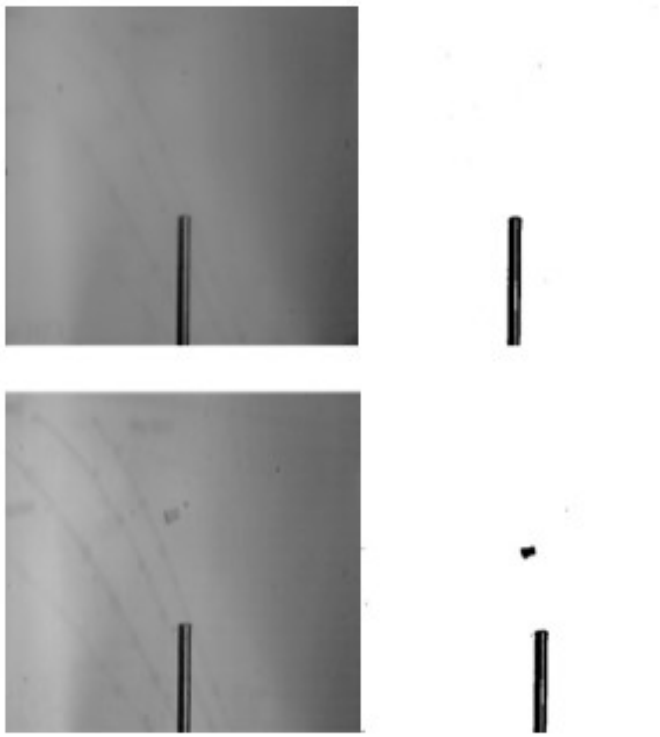

Figure 10: Examples of raw acquired images (left) and corresponding thresholded images (right).

3.3. Extraction of Breakage Parameters

After binarization of images, droplet sizes are measured before and after breakage occurs. This was achieved by using regionprops, a built in function with Matlab, which analysis the pixels within a binary image by looking for a binary picture with an 8-connected component (object). This analysis of the pixels allows for regionprops to obtain properties of the detected object which include the x- and y-coordinates of the centroid, major and minor axes of an ellipse and the radius for each droplet. Once the radius and location of the centroid are obtained from regionprops, the perimeter and areas of the droplet are calculated. To visualize the droplet shape, an ellipsoid function is generated and the ellipsoid form is calculated using the individual droplet centers and radii. Each frame of the sequence goes through the same procedure, as illustrated in the examples provided in Fig: 11 for peanut oil droplets in water.

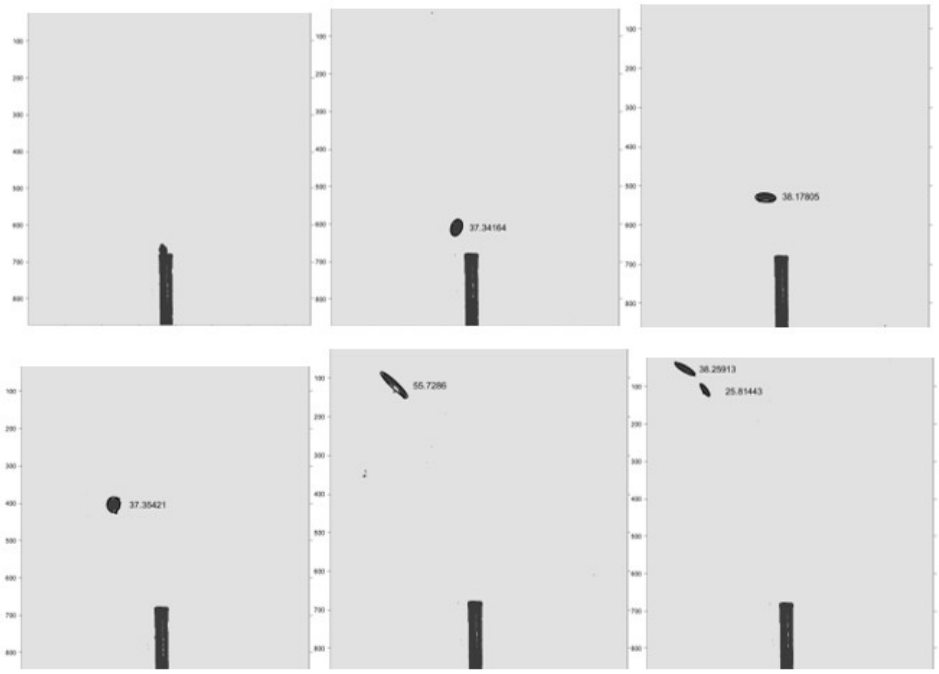

Figure 11: Sequence of peanut oil droplet breakage captured and analyzed using custom image analysis software.

In order to validate the accuracy of these ellipsoid fits to the droplet, it was prudent to validate whether the method preserves the mass of the droplet. The technique involves determining the volume of parent droplets and child droplets. The volume of ellipsoidal-shaped droplets is calculated by averaging their major and minor axes to obtain an equivalent sphere diameter, from which the droplet volume is estimated. About 650 peanut oil droplets with diameters ranging between 1.5-6 mm were injected into the von Kármán box. The volume of the child droplets was approximately 89% of the volumes of the parent droplets, which was considered acceptable given that these mass conservation calculations are based on two-dimensional images of three-dimensional objects. [23].

The authors of this methodology define breakage time as the length of time between when a droplet is released from the injection needle and when it breaks within the observation area. The initial time is defined by the frame in which the parent droplet leaves the needle tip, and time of breakage is identified by the frame in which a child droplet detaches from the parent droplet. To determine the breakage time, the number of frames between these beginning and end frames is divided by the video frame rate of 30 frames/sec. To determine breakage probabilities, the droplet data is grouped into diameter ranges using MATLAB's histogram function. Each diameter range is divided by the total number of droplets injected within that range to calculate the breakage probability. The droplet data is binned into increments of 0.3 mm, with about 100 droplets per bin.

4. Results and Discussion

4.1. Breakage Time

Figures 12 and 13 show examples of peanut oil droplets undergoing binary droplet breakage for turbulent dissipation rates of $\varepsilon = 0.083$ m^{2}s^{-3} and $\varepsilon = 0.235$ m^{2}s^{-3}, respectively. As seen in Fig: 12, the droplet leaves the tip of the needle at 0.78 seconds and undergoes breakage at 8.0 seconds. In the case of Fig: 13, the droplet leaves the tip of the needle at 0.66 seconds and undergoes breakage at 4.0 seconds (note that in Figs. 12 and 13, there are many more individual image frames in the time intervals from injection to breakage, and the six images shown represents only a small fraction of these image frames)

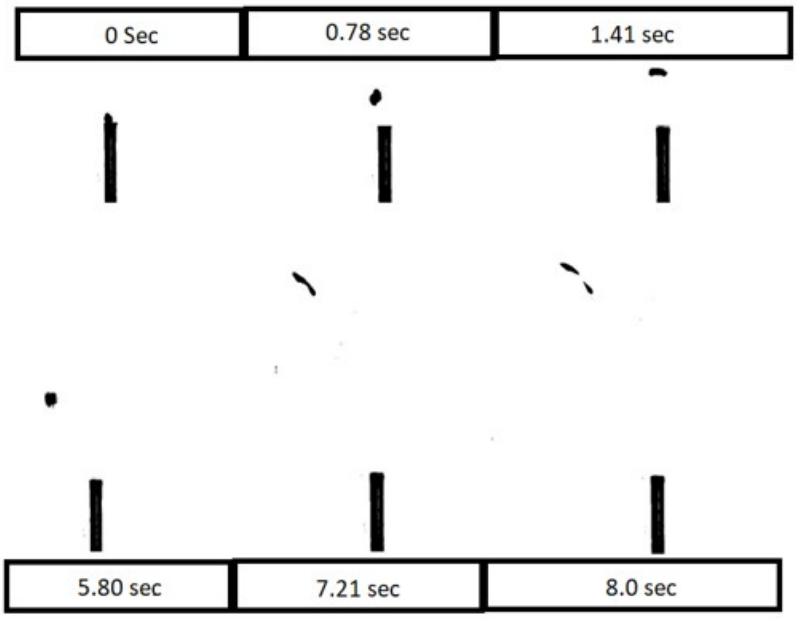

Figure 12: Sequence of peanut oil droplet breakage captured and analyzed using custom image analysis software for $\varepsilon = 0.083$ m^{2}s^{-3}.

The methodology outlined in Section 3 was employed to calculate breakage time for a large ensemble of droplets introduced into the test section through injection. The parent droplets were grouped into bins of 0.3 mm diameter increments, and a minimum of 100 distinct droplets that underwent breakage were present in each bin. Within each bin, breakage time was found to follow an approximately normal distribution. Figure 14 displays a graph of mean breakage time versus parent droplet diameter for peanut oil droplets in the von Kármán box at turbulent dissipation rates of 0.083 m^{2}s^{-3} and 0.235 m^{2}s^{-3}, respectively. The error bars in this figure represent standard errors. Generally, an increase in parent droplet diameter at a fixed dissipation rate results in a monotonic rise in breakage time. From the figure, it is also observed that an increase in the dissipation rate reduces breakage time, which is consistent with the notion that higher impeller speeds generate more

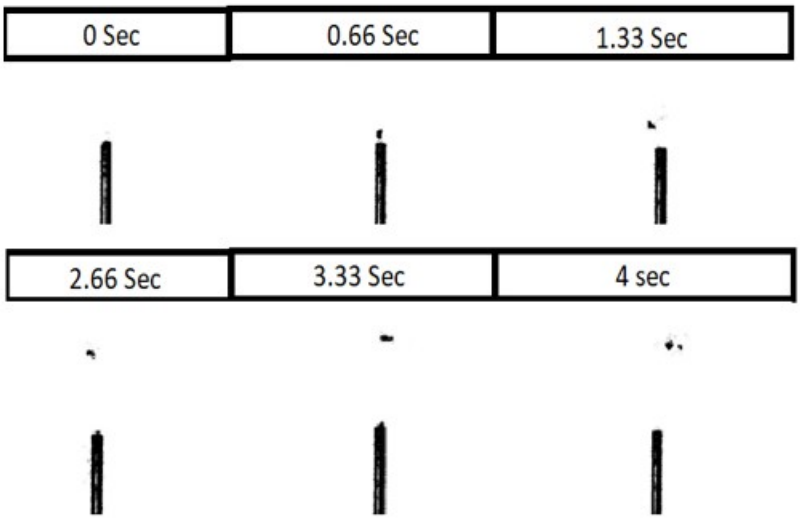

Figure 13: Sequence of peanut oil droplet breakage captured and analyzed using custom image analysis software for $\varepsilon = 0.235\ \mathrm{m^2 s^{-3}}$.

kinetic energy in turbulent eddies, resulting in more deformation stress on droplets, thereby reducing the time needed for breakage.

It is important to note that even for droplets with identical parent sizes, there can be inherent variations in the breakage time due to the probabilistic nature of the process. One other potential reason that can be attributing factor is that the flow may have small-scale fluctuations or vortices that can affect the forces acting on the droplets. These local flow conditions can introduce random variations in the deformation and breakup behavior of the droplets, leading to different breakage times. This large variation in breakage time have been observed in the works of Maab et al [8], Hero et al [9]], Solsvik et al [28].

In our previous research [7], we conducted a comparative analysis between experimental data and a theoretical model, specifically the C-T (Coulaloglou-Tavlarides) model [5]. Similarly, in the current study focusing on peanut oil droplets, we have applied the C-T model to the experimental data. This approach allows us to assess how well the C-T model conforms to the observed breakage behavior, offering valuable insights into the accuracy and suitability of this theoretical framework for the unique experimental conditions in question.

The results indicate a remarkable concurrence between the experimental data for breakage time and the predictions made by the C-T model. This strong alignment suggests that the C-T model effectively captures and represents the observed breakage behavior in our experimental findings.

4.2. Breakage Probability

To determine the probability of droplet breakage within a particular diameter range, the number of broken droplets was divided by the total number of droplets introduced into the flow cell. However, if a droplet broke before fully detaching from the injection needle

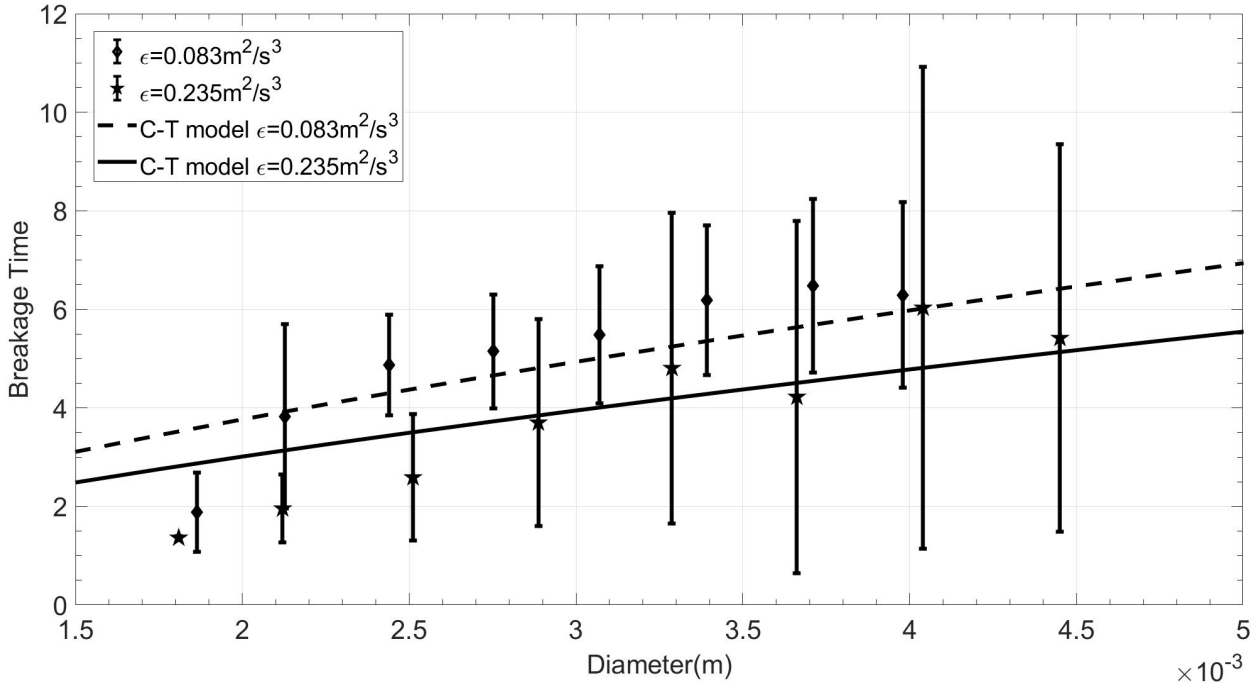

Figure 14: Breakage time vs parent droplet diameter for Peanut oil at $\varepsilon = 0.083$ and 0.235 $\mathrm{m^2 s^{-3}}$ with symbols representing experimental data and the error bars represent the standard error.The lines represent the fits to C-T Model.

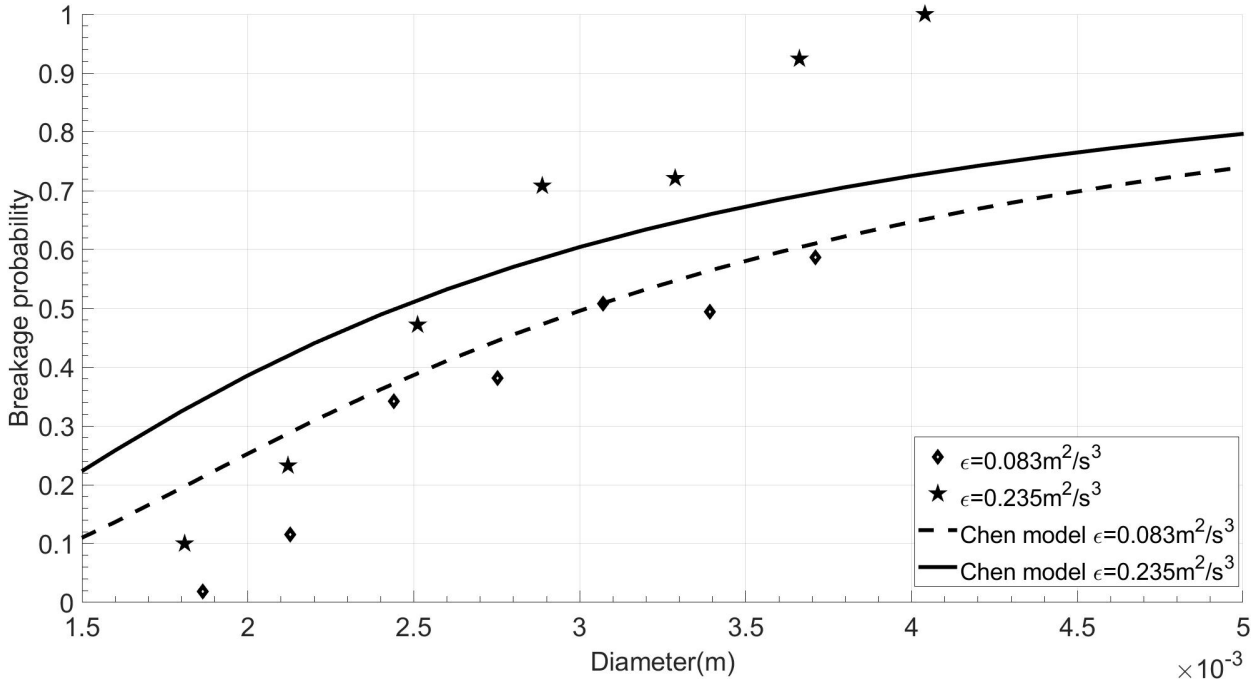

Figure 15: Breakage probability vs parent droplet diameter for peanut oil at $\varepsilon = 0.083$ and 0.235 $\mathrm{m^2 s^{-3}}$ with experimental data presented by symbols and the lines represent the fits to Chen Model.

tip, that trial was excluded from the data set. To obtain the droplet diameter bins, the major and minor ellipse axes were averaged to calculate the equivalent sphere diameter, and MATLAB's histogram function was used to group the droplets, with each bin comprising of around 100 droplets. Figure 15 presents the breakage probability of peanut oil droplets in water under turbulent dissipation rates of $\varepsilon = 0.083$ and 0.235 m^2s^{-3}, respectively. The plot shows experimental results that are consistent with the expectation that the probability of breakage increases with both increasing parent droplet size and turbulent dissipation rate.

In our earlier research[7], we conducted a comprehensive examination by comparing our experimental data with a theoretical model, specifically the Chen model [6]. Similarly, in our current study focusing on peanut oil droplets, we have employed the Chen model to analyze our experimental data, this time with a focus on evaluating its compatibility with the observed breakage probability patterns. This approach allows us to gain valuable insights into how well the Chen model aligns with the actual breakage probability trends under the specific experimental conditions we are exploring.

The outcomes reveal a notable agreement between the experimental breakage probability data and the predictions made by the Chen model. This strong correspondence suggests that the Chen model effectively represents and characterizes the observed breakage probability behavior within our experimental results.

4.3. Breakage Rate

The breakage rate coefficient "a" in Eq. (1) can be computed from the experimental data by dividing the breakage probability by breakage time. Figure 15 shows the breakage rate of peanut oil at turbulence dissipation rates of $\varepsilon = 0.083$ and $0.235 m^2 s^{-3}$, respectively. The breakage rate is seen to increase to a peak breakage rate before decreasing to an asymptote as the parent droplet diameter increases. Similar to breakage probability, the breakage rate increases with an increase in turbulence dissipation rate.

4.4. Child Distribution Function

The child distribution refers to the likelihood that a droplet of a specific diameter d results from the breakage of a mother droplet with a diameter D. Ravichandar et al [7, 25] noted that the child distribution function can be expressed using the following equation:

$$\int_0^q pb(p|q)\partial p = q \tag{5}$$

where $b(p|q)$ is the conditional probability that a child droplet with volume p is produced upon breakage of a parent droplet with volume q. The theoretical shape of the distribution of the daughter size droplets is commonly examined under the assumption of binary breakage and indeed binary breakage was observed during the experimental investigation. In this research, the probability density function (pdf) employed assumes a specific focus on a single droplet resulting from binary breakup, without consideration of the initial droplet undergoing breakup. It is worth noting that adopting an alternative perspective centered on the initial droplet would involve the inclusion of two child droplets in the binary breakup

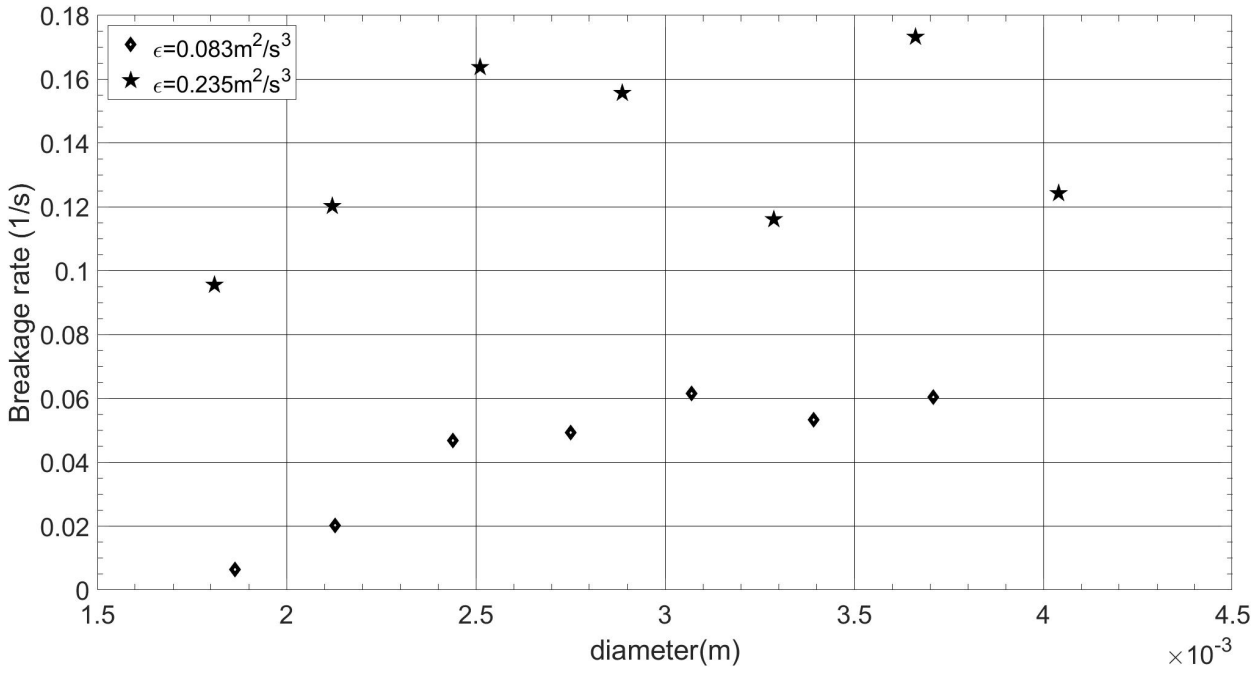

Figure 16: Breakage rate vs parent droplet diameter for Peanut oil at $\varepsilon = 0.083$ and $0.235 m^2 s^{-3}$ with symbols representing experimental data and the error bars represent the standard error

scenario. However, the chosen frame of reference for this study pertains to the post-breakup phase, where the aim is to characterize the size distribution of the resultant child droplets. This approach ensures that the summation of probabilities assigned to the diameters of a single child droplet equates to one, reflecting the commitment to a comprehensive analysis of droplet dynamics after breakup. The manuscript has been diligently revised to provide further clarity on this matter.

Figures 17 and 18 show the child distribution function for peanut oil as fractions of the parent droplet volume, across different parent droplet diameters. About 100 droplet breakage events were recorded for peanut oil at $\varepsilon = 0.083$ and 0.235 $\mathrm{m^2 s^{-3}}$. For $\varepsilon = 0.083$ $\mathrm{m^2 s^{-3}}$, the distributions appear to be monomodal, with a preference for equally-sized child droplets for smaller parent droplets, especially for the smaller droplet diameters. However, it is apparent that increasing the parent droplet size increases the likelihood of unequal child droplet sizes, as seen in Fig: 17c and d when compared to Fig: 17a and b . Furthermore, increasing turbulent dissipation from $\varepsilon = 0.083$ to 0.235 $\mathrm{m^2 s^{-3}}$ for the same parent droplet size, as depicted in Fig: 18, results in the child distribution function shifting to a bimodal distribution from a monomodal distribution. This can be the cause of the deformation stress surpassing the stabilization stress significantly, resulting in droplets undergoing significant deformation, which leads to the production of unequally-sized child droplets.

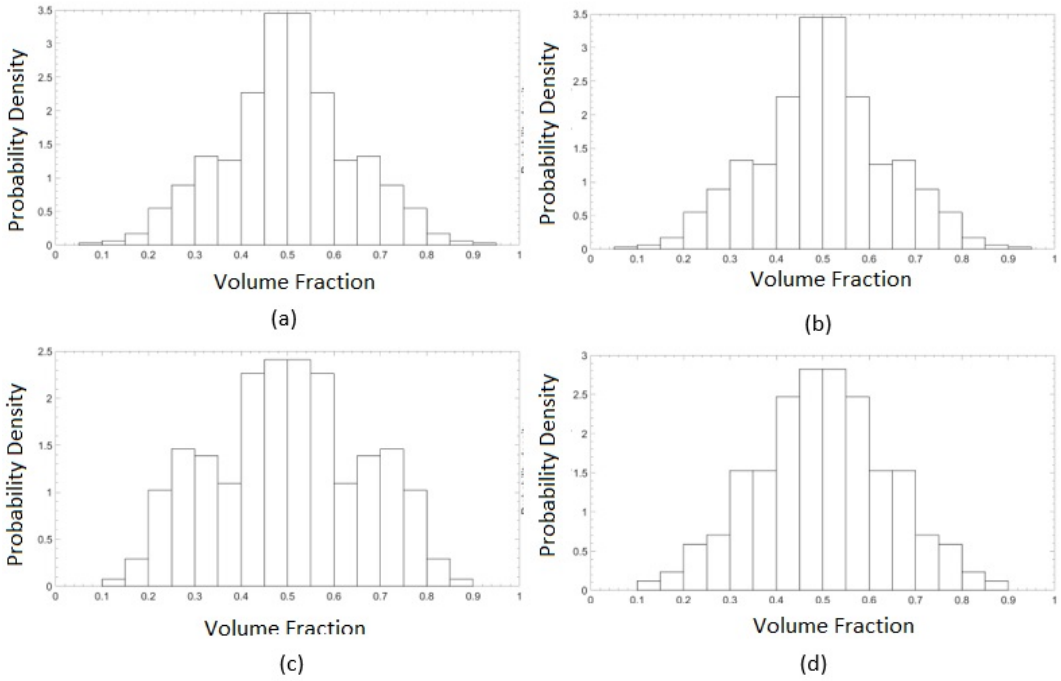

Figure 17: Peanut oil daughter droplet size distribution for $\varepsilon = 0.083$ m^{2}s^{-3}, for parent droplet diameters of (a) 1.9 mm, (b) 2.6 mm, (c) 3.3 mm, (d) 3.9 mm.

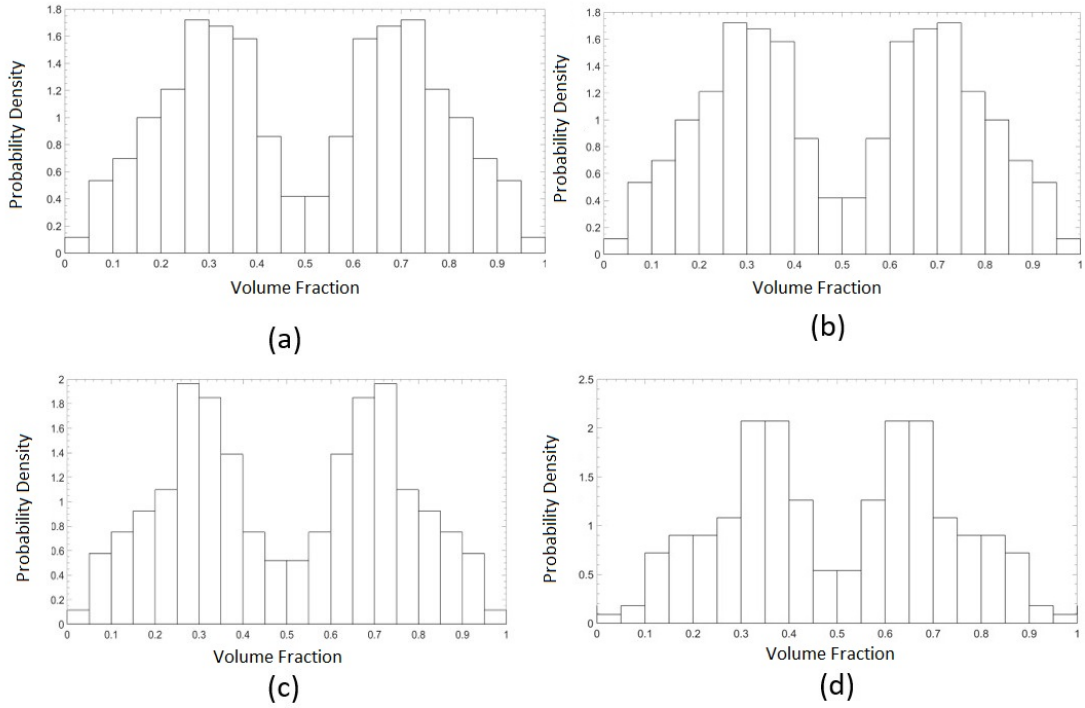

Figure 18: Peanut oil daughter droplet size distribution for $\varepsilon = 0.235$ m^{2}s^{-3}, for parent droplet diameters of (a) 1.9 mm, (b) 2.7 mm, (c) 3.5 mm, (d) 4.7 mm.

5. Summary and Conclusions

Droplet breakup in liquid-liquid dispersions involves complicated phenomena that have not yet been adequately clarified to allow for dependable models.Even among existing models of the droplet breakage phenomenon, the validation of these models has been hindered by a lack of experimental data gathered under well controlled and characterized conditions. Accordingly, significant efforts are still needed to gather experimental data that will help us better explain the mechanisms behind the droplet breakage processes.

One of the major limitations of existing experimental investigations into droplet breakage is that they have been performed using stirred tanks or other devices that generate heterogeneous turbulence. This makes it difficult to accurately determine the turbulent dissipation rate responsible for the droplet breakage.Another limitation is the difficulty of gathering sufficient data to resolve important droplet breakage features such as breakage time, breakage probability, and child droplet probability distribution functions.

To overcome these limitations a von Kármán swirling flow device was developed to carry out droplet breakage studies in a homogeneous turbulent flow using optical methods for acquiring breakage data. The symmetrical flow apparatus has inside dimensions 200.15 mm x 250.95 mm x 206.502 mm and counter-rotating impellers of 200 mm diameter fitted to the opposite sides of the test section. Within the breakage observation volume, turbulent dissipation rate is nearly constant, based on 3-dimensional computational fluid dynamics simulations.

The von Kármán test section and experimental methodology were demonstrated by performing experiments on the breakage of peanut oil droplets in water. The process for extracting breakage data from video image frames was explained, and the definitions and physical interpretations of various quantities characterizing breakage were provided. Using the device and methodology, it was shown that quantities such as parent and child droplet diameter, breakage time and breakage probability can be measured from a large ensemble of individual breakage events. Additionally, a droplet production process was developed so that the von Kármán flow cell could be repeatedly injected with individual parent droplets of various sizes. Using the von Kármán flow cell and droplet generation methodology, it is possible to gain independent control of the turbulent dissipation rate and the parent droplet size - two crucial elements that affect droplet breakage.

The investigation demonstrated the ability to collect a significant number of droplet breakage events, which could be used to obtain important droplet breakage parameters. The analysis of breakage events for peanut oil revealed that larger parent droplets had higher breakage probability and longer breakage time. Furthermore, increasing the tubulent dissipation rate was found to increase the overall breakage probability but decrease the breakage time.

The child droplet distributions of peanut oil exhibit a monomodal pattern, with a significant inclination towards the formation of child droplets of uniform size. As the turbulent dissipation rate increase for the same-sized parent droplet, there is a slow transition to a bimodal distribution from a monomodal distribution. This can be due to the deformation stress surpassing the stabilization stress, resulting in the droplet undergoing significantly

more deformation and leading to the parent droplet breaking unevenly.

Acknowledgement

This work was funded by grant CBET-2201707 from the National Science Foundation.

References

[1] Ashar, M., Arlov, D., Carlsson, F., Innings, F., & Andersson, R. (2018). Single droplet breakup in a rotor-stator mixer. Chemical Engineering Science, 181, 186–198. doi:10.1016/j.ces.2018.02.021

[2] Andersson, R., & Andersson, B. (6 2006). On the breakup of fluid particles in turbulent flows. AIChE Journal, 52, 2020–2030. doi:10.1002/aic.10831

[3] Ronnie Andersson, & Bengt Andersson (2006). Modeling the breakup of fluid particles in turbulent flows. AIChE Journal, 52.

[4] Argyropoulos, C. D., & Markatos, N. C. (2015). Recent advances on the numerical modelling of turbulent flows. Applied Mathematical Modelling, 39. doi:10.1016/j.apm.2014.07.001

[5] Coulaloglou, C. A., & Tavlarides, L. L. (1977). Description of interaction processes in agitated liquid-liquid dispersions. In Chemical Engineering Science (Vol. 32, Issue 11, pp. 1289–1297). Elsevier BV. https://doi.org/10.1016/0009-2509(77)85023-9

[6] Chen, Z., Prüss, J., & Warnecke, H.-J. (1998). A population balance model for disperse systems. In Chemical Engineering Science (Vol. 53, Issue 5, pp. 1059–1066). Elsevier BV. https://doi.org/10.1016/s0009-2509(97)00328-x

[7] Ravichandar, K., Vigil, R. D., Fox, R. O., Nachtigall, S., Daiss, A., Vonka, M., & Olsen, M. G. (2022). Turbulent droplet breakage in a von Kármán flow cell. Physics of Fluids, 34(7), 073319. doi:10.1063/5.0096395

[8] Maaß, S., & Kraume, M. (3 2012). Determination of breakage rates using single drop experiments. Chemical Engineering Science, 70, 146–164. doi:10.1016/j.ces.2011.08.027

[9] Herø, E. H., Forgia, N. L., Solsvik, J., & Jakobsen, H. A. (11 2020). Single drop breakage in turbulent flow: Statistical data analysis. Chemical Engineering Science: X, 8. doi:10.1016/j.cesx.2020.100082

[10] Feng, H., Olsen, M. G., Liu, Y., Fox, R. O., & Hill, J. C. (2005). Investigation of turbulent mixing in a confined planar-jet reactor. AIChE Journal, 51. doi:10.1002/aic.10527

[11] Forgia, N. L., Herø, E. H., & Jakobsen, H. A. (2021). High-speed image processing of fluid particle breakage in turbulent flow. Chemical Engineering Science: X, 12. doi:10.1016/j.cesx.2021.100117

[12] Galinat, S., Masbernat, O., Guiraud, P., Dalmazzone, C., & Noïk, C. (2005). Drop break-up in turbulent pipe flow downstream of a restriction. Chemical Engineering Science, 60. doi:10.1016/j.ces.2005.05.012

[13] Galinat, S., Torres, L. G., Masbernat, O., Guiraud, P., Risso, F., Dalmazzone, C., & Noik, C. (2007). Breakup of a drop in a liquid-liquid pipe flow through an orifice. AIChE Journal, 53. doi:10.1002/aic.11055

[14] Eirik H. Herø, Nicolas La Forgia, Jannike Solsvik, & Hugo A. Jakobsen (2020). Single drop breakage in turbulent flow: Statistical data analysis. Chemical Engineering Science: X, 8.

[15] Zambrano, H. M. D. L. R., Verhille, G., & Gal, P. L. (2018). Fragmentation of magnetic particle aggregates in turbulence. Physical Review Fluids, 3. doi:10.1103/PhysRevFluids.3.084605

[16] Li, C., Miller, J., Wang, J., Koley, S. S., & Katz, J. (2017). Size Distribution and Dispersion of Droplets Generated by Impingement of Breaking Waves on Oil Slicks. Journal of Geophysical Research: Oceans, 122. doi:10.1002/2017JC013193

[17] Liu, Y., Olsen, M. G., & Fox, R. O. (2009). Turbulence in a microscale planar confined impinging-jets reactor. Lab on a Chip, 9. doi:10.1039/b818617k

[18] D. Maggioris, A. Goulas, A. H. Alexopoulos, E. G. Chatzi, & C. Kiparissides (2000). Prediction of particle size distribution in suspension polymerization reactors: Effect of turbulence nonhomogeneity. Chemical Engineering Science, 55.

[19] Marchetti, J. M., & Svendsen, H. F. (2012). Review of Kernels for Droplet-Droplet Interaction, Droplet-Wall Collision, Entrainment, Re-entrainment, and Breakage. Chemical Engineering Communications, 199. doi:10.1080/00986445.2011.592453

[20] McClements, D. J. (1999). Food Emulsions and Foams: Interfaces, Interactions and Stability, Edited by E. Dickinson and J.M. Rodriguez, The Royal Society of Chemistry, Cambridge, 1999, pp. 390, ISBN 0-85404-753-0, UK £85.00. Colloids and Surfaces A: Physicochemical and Engineering Aspects, 160. doi:10.1016/s0927-7757(99)00231-9

[21] Meslem, A., Bode, F., Croitoru, C., & Nastase, I. (2014). Comparison of turbulence models in simulating jet flow from a cross-shaped orifice. European Journal of Mechanics, B/Fluids, 44. doi:10.1016/j.euromechflu.2013.11.006

[22] Nachtigall, S., Zedel, D., & Kraume, M. (2 2016). Analysis of drop deformation dynamics in turbulent flow. Chinese Journal of Chemical Engineering, 24, 264–277. doi:10.1016/j.cjche.2015.06.003

[23] Ganesan Narsimhan, Gregory Nejfelt, & Doraiswami Ramkrishna (1984). Breakage functions for droplets in agitated liquid-liquid dispersions. AIChE Journal, 30.

[24] Nissanka, I. D., & Yapa, P. D. (2018). Calculation of oil droplet size distribution in ocean oil spills: A review. Marine Pollution Bulletin, 135. doi:10.1016/j.marpolbul.2018.07.048

[25] Krishnamurthy Ravichandar, Michael G. Olsen, & R. Dennis Vigil (2023). Turbulent droplet breakage probability: Analysis of fitting parameters for two commonly used models. Chemical Engineering Science, 266, 118311.

[26] Sajjadi, B., Raman, A. A. A., Shah, R. S. S. R. E., & Ibrahim, S. (6 2013). Review on Applicable breakup/coalescence models in turbulent liquid-liquid flows. Reviews in Chemical Engineering, 29, 131–158. doi:10.1515/revce-2012-0014

[27] Sathyagal, A. N., Ramkrishna, D., & Narsimhan, G. (1996). Droplet breakage in stirred dispersions. breakage functions from experimental drop-size distributions. Chemical Engineering Science, 51. doi:10.1016/0009-2509(95)00311-8

[28] Solsvik, J., & Jakobsen, H. A. (2 2016). Development of Fluid Particle Breakup and Coalescence Closure Models for the Complete Energy Spectrum of Isotropic Turbulence. Industrial and Engineering Chemistry Research, 55, 1449–1460. doi:10.1021/acs.iecr.5b04077

[29] Solsvik, J., Tangen, S., & Jakobsen, H. A. (2013). Reviews in Chemical Engineering, 29(5), 241–356. doi:10.1515/revce-2013-0009

[30] Zhou, W., Hu, J., Feng, M., Yang, B., & Cai, X. (2015). Study on imaging method for measuring droplet size in large sprays. Particuology, 22. doi:10.1016/j.partic.2014.12.003

[31] Verhille, G., Plihon, N., Bourgoin, M., Odier, P., & Pinton, J.-F. (2010). Induction in a von Kármán flow driven by ferromagnetic impellers. New Journal of Physics, 12(3), 033006. doi:10.1088/1367-2630/12/3/033006

[32] Ravelet, F., Chiffaudel, A., & Daviaud, F. (2008). Supercritical transition to turbulence in an inertially driven von Kármán closed flow. Journal of Fluid Mechanics, 601, 339–364. doi:10.1017/S0022112008000712

[33] Fauve, S., Dormy, E., Gissinger, C., & Pétrélis, F. (2009). Reversals of the magnetic field generated by a turbulent flow. In B. Eckhardt (Ed.), Advances in Turbulence XII (pp. 801–808). Berlin, Heidelberg: Springer Berlin Heidelberg.

[34] Volk, R., Odier, P., & Pinton, J.-F. (2005). Fluctuation of magnetic induction in von Kármán swirling flows. Physics of Fluids, 18, 085105.

[35] Berning, H., & Rösgen, T. (2023). Suppression of large-scale azimuthal modulations in a von Kármán flow using random forcing. In Physics of Fluids (Vol. 35, Issue 7). AIP Publishing. https://doi.org/10.1063/5.0152876

[36] Zhou, H., Yu, X., Wang, B., Jing, S., Lan, W., & Li, S. (2022). Breakup model of oscillating drops in turbulent flow field. In Chemical Engineering Science (Vol. 247, p. 117036). Elsevier BV. https://doi.org/10.1016/j.ces.2021.117036

[37] Zhou, H., Yu, X., Wang, B., Jing, S., Lan, W., & Li, S. (2020). Experimental study on drop breakup time and breakup rate with drop swarms in a stirred tank. In AIChE Journal (Vol. 67, Issue 1). Wiley.

https://doi.org/10.1002/aic.17065
[38] Yu, X., Li, S., Zhou, H., Jing, S., Lan, W., & Li, S. (2020). Numerically simulating droplet breakup in droplet swarm using modified level set method with multi-levels. In Chemical Engineering Science (Vol. 211, p. 115263). Elsevier BV. https://doi.org/10.1016/j.ces.2019.115263
[39] Simon, M., Schmidt, S. A., & Bart, H.-J. (2003). The Droplet Population Balance Model – Estimation of Breakage and Coalescence. In Chemical Engineering & Technology (Vol. 26, Issue 7, pp. 745–750). Wiley. https://doi.org/10.1002/ceat.200306101